Computational Mechanics manuscript No.
(will be inserted by the editor)

An effective meshfree reproducing kernel method for buckling analysis of cylindrical shells with and without cutouts

S. Sadamoto · M. Ozdemir · S. Tanaka · K. Taniguchi · T.T. Yu · T.Q. Bui

Received: date / Accepted: date

Abstract The paper is concerned with eigen buckling analysis of curvilinear shells with and without cutouts by an effective meshfree method. In particular, shallow shell, cylinder and perforated cylinder buckling problems are considered. A Galerkin meshfree reproducing kernel (RK) approach is then developed. The present meshfree curvilinear shell model is based on Reissner-Mindlin plate formulation, which allows the transverse shear deformation of the curved shells. There are five degrees of freedom per node (*i.e.*, three displacements and two rotations). In this setting, the meshfree interpolation functions are derived from the RK. A singular kernel is introduced to impose the essential boundary conditions because of the RK shape functions, which do not automatically possess the Kronecker delta property. The stiffness matrix is derived using the stabilized conforming nodal integration technique. A convected coordinate system is introduced into the formulation to deal with the curvilinear surface. More importantly, the RKs taken here are used not only for the interpolation of the curved geometry, but also for the approximation of field variables. Several numerical examples with shallow shells and full cylinder models are considered, and the critical buckling loads and their buckling mode shapes are calculated by the meshfree eigenvalue analysis and examined. To show the accuracy and performance of the developed meshfree method, the computed critical buckling loads and mode shapes are compared with reference solutions based on boundary domain element, finite element and analytical methods.

Keywords Meshfree Method · Reproducing Kernel · Cylindrical Shell · Buckling · Convected Coordinate System

S. Sadamoto, S. Tanaka, K. Taniguchi
Graduate School of Engineering, Hiroshima University, 4-1, Kagamiyama 1-chome, Higashi-Hiroshima,739-8527, Japan
Tel.: +81-82-424-7859
Fax: +81-82-422-8527
E-mail: satoyuki@hiroshima-u.ac.jp

S.Sadamoto
E-mail: shota.sadamoto@gmail.com

K.Taniguchi
E-mail: m166479@hiroshima-u.ac.jp

M. Ozdemir
Faculty of Naval Architecture and Ocean Engineering, Istanbul Technical University, Turkey
Faculty of Marine Science, Ordu University, Turkey
E-mail: mozdemir@itu.edu.tr

T.T. Yu
Department of Engineering Mechanics, Hohai University, China
E-mail: tiantangyu@hhu.edu.cn

T.Q. Bui
Department of Civil and Environmental Engineering, Tokyo Institute of Technology, Japan
E-mail: tinh.buiquoc@gmail.com

1 Introduction

Tubular members are main components in offshore, civil and aerospace structures because of their high strength-to-weight ratio and high resistance to hydrostatic pressure. Engineers and researchers are concerned with the structural stability of thin-walled tubular sections. The load bearing capacity of these structures is strongly related to their buckling capacity. Therefore, the buckling strength of tubular structures must be assessed from the viewpoint of structural safety. The finite element

method (FEM) is a technique commonly used to simulate the buckling collapse of tubular members [1]–[8] and other structural components in offshore structures, such as plates, stiffened plate structures and hull girders [9]–[15]. However, difficulties may arise in the modeling of curved surfaces because the curved surface is generally modeled by an assembly of flat plate elements. In addition, there may be shear locking phenomenon owing to the linear nature of the finite elements (FEs), such that the structural model may seem stiffer than the actual structure. There have been several developments of FE formulations and discretizations including higher-order FEs to overcome such shear locking problems, see Refs.[16] and [17].

In the last two decades, new methodologies for analyzing boundary value problems have been introduced including meshfree methods [18]–[23], isogeometric analysis [24]–[28] and wavelet Galerkin methods [29]–[33]. Continuous stress and strain fields can be obtained by adopting smooth functions to approximate the field variables, which is advantageous in solving solid and structural problems. In the case of meshfree Galerkin methods, Krysl and Belytschko [34], [35] analyzed thin plate and shell problems employing the element-free Galerkin method (EFGM) and adopting a quadratic or higher-order polynomial basis to meet consistency requirements. The membrane locking of shells was addressed by enlarging the influence domain of the meshfree interpolation functions. The first attempt to employ three-dimensional (3D) reproducing kernel particle method (RKPM) to solve structural problems was Li *et al.* [36]. In this article, large deformation of thin shell structures was handled by 3D reproducing kernel (RK) functions with an explicit solution scheme. Noguchi *et al.* [37] analyzed shell and 3D spatial structures employing the EFGM and a convected coordinate system. Additionally, Kanok-Nukulchai *et al.* [38] implemented the concept of matching fields in the EFGM to eliminate shear locking problems for shear-deformable beams and plates. Zhang *et al.* [39] examined shell structures with slope discontinuities employing a moving least-squares approximation with discontinuous derivative basis functions. Tanaka *et al.* [40]–[42] treated discontinuous displacements along a crack segment with the diffraction method and a visibility criterion [43], [44] on the basis of the RKPM [19]–[23].

Unlike the meshfree analysis of flat plates and shells, the analysis of cylindrical shells employing meshfree methods is relatively rare. Yiotis and Katsikadelis [45] examined linear buckling behaviors of cylindrical shell panels employing a meshless analog equation method, which is based on the principle of an analog equation. In addition, Wang *et al.* [46] proposed a circumferentially enhanced meshfree method based on the Hermite RK approximation [47]–[51] for the buckling analysis of Kirchhoff–Love cylindrical shells. In the meshfree formulation, a mapping technique between Cartesian and cylindrical coordinate systems was used. Periodical mode shapes of the cylinders were captured. Failure analysis of cylindrical shells has also been addressed in the literature; *i.e.*, Qian *et al.* [52] simulated collapse modes of cylindrical shells under internal pressure and thermal loads employing a meshfree Galerkin approach. Meanwhile, Zhao *et al.* [53], [54] reported the free vibration analysis of cylindrical shells using meshfree methods. The authors of the present study previously carried out geometrical nonlinear analyses for plate and stiffened plate structures [55]–[57]. In the literatures, post-buckling structural responses were examined by elastic large deflection analysis and were compared with the FEM results for flat plate case [55], flat plate with initial imperfection [56] and folded plate structures [57]. And, it was confirmed that the presented meshfree method have good accuracy for predicting post-buckling behaviors.

Buckling/ultimate capacity of structures is mostly determined by elastic and elasto-plastic large deflection analyses, respectively. However, prediction of theoretical buckling loads and modes has also crucial importance. In that respect, the main purpose of this study is to conduct eigen buckling analysis of cylindrical shells under longitudinal compression using the meshfree RK approximation. A convected coordinate system is introduced to treat general curved surfaces and can be used in structural modeling with arbitrary geometries; *e.g.*, perforated cylinders and curved stiffened plates. The RKs are employed to interpolate the curved geometry and approximate field variables on curved shells. The membrane deformation is assumed to have a plane stress condition, while the Mindlin–Reissner plate formulation is adopted for out-of-plane deformation. When evaluating the stiffness matrix, stabilized conforming nodal integration (SCNI) [58], [59] is employed. Because not only curved surface geometry but also the field variable can be approximated using the meshfree functions, the present approach utilized for analyzing structural buckling problems including arbitral curved surface geometry. Additionally, meshfree eigen buckling analysis adopting higher-order interpolation functions with advanced numerical integration technique; *e.g.*, SCNI is mostly superior to linear FEs to overcome shear locking problem. The meshfree Galerkin discretization of the curved shells considers five degrees of freedom (DOF) per node. As for imposition of the essential boundary conditions (BCs), several discretization techniques have been proposed

and implemented; *i.e.*, Lagrange multiplier method [34], [35], penalty method [37] and multiple point constraint (MPC) method [55]–[57]. However, a previous study conducted by the present authors showed that adopting the MPC technique in the meshfree Galerkin method produces small stress oscillations along the boundaries [55]. A robust essential BC enforcement technique is required in the linear buckling analysis to evaluate the buckling loads and modes with high accuracy for the cylindrical shell models. Therefore, a singular kernel (SK) [60] is introduced to impose the so-called Kronecker delta property in the set of the meshfree interpolants. Buckling characteristic of shallow and cylindrical shells strongly depends on discretization and element formulation. Therefore, only critical loads and their mode shapes are studied.

The rest of the paper is organized as follows. A shear-deformable curved shell formulation using a convected coordinate system is presented in Section 2. The meshfree discretization, numerical integration for the stiffness matrix and imposition of essential BCs are detailed in Section 3. Section 4 presents numerical examples of shallow shells, full cylinder models and perforated cylinder buckling problems, and compares the results obtained with reference solutions. Main conclusions are drawn in Section 5.

2 Meshfree curved shell formulation

2.1 Kinematic of shells

The mapping techniques between Cartesian and convected coordinate systems for curvilinear shells and 3D spatial structures were examined in detail by Noguchi *et al.* [37] and the present authors [56], [57] for geometrical nonlinear formulation based on the total Lagrangian method. In a similar manner, a mapping algorithm is introduced in the present paper to transform the curved shell geometry to the equivalent two-dimensional space and vice-versa for the analysis of buckling modes and loads of the curved shell structures.

A schematic illustration of the mapping technique for Cartesian and convected coordinate systems is shown in Fig.1(a). $\boldsymbol{X}$=(X_1, X_2, X_3) is a position vector in the Cartesian coordinate system, while $\boldsymbol{r}$=(r^1, r^2, r^3) is that in the convected one. The physical values in the two coordinate systems have one-to-one correspondence. The field variables in each coordinate system can be transformed through the convected coordinate system. A curved shell geometry is illustrated in Fig.1(b). The r^1–r^2 is a mid-thickness plane of the curved shell. The curved shell has a uniform thickness t_h throughout the analysis domain. $\boldsymbol{e}_i$ (i=1,2,3) is an orthogonal unit vector in the Cartesian coordinate system that corresponds to the X_i-axis. $\boldsymbol{V}_i$ is an orthogonal unit vector on the mid-thickness plane. The unit vectors $\boldsymbol{V}_1$, $\boldsymbol{V}_2$ and $\boldsymbol{V}_3$ have the relation,

$$\boldsymbol{V}_2 = \frac{\boldsymbol{V}_3 \times \boldsymbol{e}_1}{|\boldsymbol{V}_3 \times \boldsymbol{e}_1|}, \tag{1}$$

$$\boldsymbol{V}_1 = \boldsymbol{V}_2 \times \boldsymbol{V}_3. \tag{2}$$

A thick shell is assumed in the present curved shell formulation. Mindlin–Reissner plate theory is adopted to allow transverse shear deformation of the curved shell. A homogeneous isotropic elastic material is assumed.

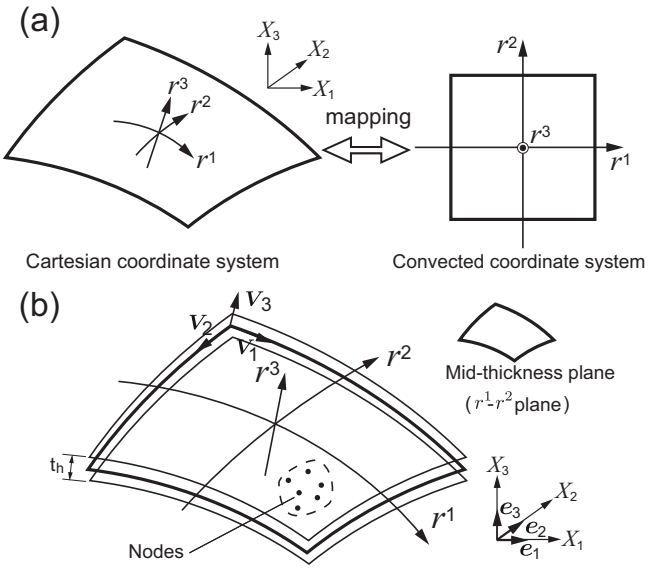

Fig. 1 A schematic illustration of convected coordinate system: **a** mapping system for a curvilinear geometry, **b** a curved shell geometry and its meshfree discretization

When considering the curved shell problems as indicated in Fig.1(b), a position vector $\boldsymbol{X}$ on the curved shell is defined by

$$\boldsymbol{X} = \boldsymbol{X}_\mathrm{mid} + \frac{r^3}{2} t_\mathrm{h} \boldsymbol{V}_3, \tag{3}$$

where $\boldsymbol{X}_\mathrm{mid}$ is a position vector on the mid-thickness plane of the curved shell in the Cartesian coordinate system, while $\boldsymbol{V}_3$ is a directional unit vector (director) normal to the mid-thickness plane. Similarly, the translation of an arbitrary point on the curved shell can be evaluated in terms of a displacement vector $\boldsymbol{u}$ as:

$$\boldsymbol{u} = \boldsymbol{u}_\mathrm{mid} + \frac{r^3}{2} t_\mathrm{h} (-\theta_1 \boldsymbol{V}_2 + \theta_2 \boldsymbol{V}_1), \tag{4}$$

where θ_1 and θ_2 are rotation components in terms of the tangential unit vectors $\boldsymbol{V}_1$ and $\boldsymbol{V}_2$ on the mid-thickness

plane, respectively. The term $-\theta_1 \boldsymbol{V}_2 + \theta_2 \boldsymbol{V}_1$ in Eq.(4) corresponds to rotation of the director $\boldsymbol{V}_3$.

2.2 Mathematical representations of the curved shell geometry and the deformation

A five-DOF flat shell formulation based on RKs and SCNI was developed by Wang and Sun [61] and the present authors [55]. Shear-deformable flat shell modeling based on RKs and SCNI can overcome the shear locking problem by imposing the so-called Kirchhoff mode reproducing condition [62], [63]. The curved shell formulation and the discretization are performed as in the previous works.

In the meshfree Galerkin discretization of curved shells, the RKs are used not only for the curved geometry interpolation, but also for the field variables approximation. The basic concept is the same as that of the isoparametric FEM. The completeness condition can thus be satisfied in the meshfree analysis. Nodes are distributed on the mid-thickness plane as shown in Fig.1(b) and the orthogonal unit vector $\boldsymbol{V}_i$ is defined at each node; *i.e.*, $\boldsymbol{V}_{iI}$ for the I-th node. A position vector $\boldsymbol{X}_{\rm mid}(r^1, r^2)$ on the mid-thickness plane (r^1–r^2 plane) of the curved shell is interpolated using the RKs as:

$$\boldsymbol{X}_{\rm mid}(r^1, r^2) = \sum_{I=1}^{\rm NP} \psi_I(r^1, r^2) \boldsymbol{X}_{{\rm mid}I}, \tag{5}$$

where $\psi_I(r^1, r^2)$ and $\boldsymbol{X}_{{\rm mid}I}$ are the RK and position vector of the I-th node on the mid-thickness plane, respectively. NP is the total number of scattered nodes used for the interpolation of the mid-thickness plane of the curved shell. The positon vector of an arbitrary point on the curved shell $\boldsymbol{X}(\boldsymbol{r})(=\boldsymbol{X}(r^1, r^2, r^3))$ is then written as

$$\boldsymbol{X}(\boldsymbol{r}) = \sum_{I=1}^{\rm NP} \psi_I(r^1, r^2) \left(\boldsymbol{X}_{{\rm mid}I} + \frac{r^3}{2} t_{\rm h} \boldsymbol{V}_{3I} \right), \tag{6}$$

where $\boldsymbol{V}_{3I}$ is a director of the I-th node. The RK on the mid-thickness plane $\psi_I(r^1, r^2)(=\psi_I)$ can be written as:

$$\psi_I = \boldsymbol{h}^T(r_I^1 - r^1, r_I^2 - r^2) \boldsymbol{b}(r^1, r^2) \phi_I(r_I^1 - r^1, r_I^2 - r^2), \tag{7}$$

where $\boldsymbol{h}(r_I^1 - r^1, r_I^2 - r^2)$ and $\boldsymbol{b}(r^1, r^2)$ are the basis vector and coefficient vector, respectively. A complete quadratic basis is chosen as the basis vector; *i.e.*,

$$\boldsymbol{h}(r_I^1 - r^1, r_I^2 - r^2) = \{ 1 \; r^1 \; r^2 \; (r^1)^2 \; r^1 r^2 \; (r^2)^2 \}. \tag{8}$$

Additionally, the coefficient vector $\boldsymbol{b}(r^1, r^2)$ is determined so as to satisfy the reproducing condition:

$$\sum_{I=1}^{\rm NP} \psi_I(r_I^1)^i (r_I^2)^j = (r^1)^i (r^2)^j, \quad (0 \le i + j \le 2). \tag{9}$$

In Eq.(7), $\phi_I(r_I^1 - r^1, r_I^2 - r^2)(=\phi_I)$ is an original kernel for constructing the RKs. A cubic spline function is chosen:

$$\phi_I = \frac{10}{7\pi h^2} \begin{cases} 1 - \frac{3}{2} s_I^2 + \frac{3}{4} s_I^3 & (0 \le s_I \le 1) \\ \frac{1}{4}(2 - s_I)^3 & (1 \le s_I \le 2) \\ 0 & (2 \le s_I) \end{cases}, \tag{10}$$

where h is a parameter that defines the function support, and $s_I = \sqrt{(r_I^1 - r^1)^2 + (r_I^2 - r^2)^2}/h$ is the normalized distance from the center of the kernel.

The displacement vector $\boldsymbol{u} = \{u_1 \; u_2 \; u_3\}^T$ of an arbitrary point on the curved shell is approximated using the RKs as:

$$\begin{aligned} \boldsymbol{u} &= \begin{Bmatrix} u_{\rm mid1} - \frac{t_{\rm h}}{2} r^3 \theta_1 V_{21} + \frac{t_{\rm h}}{2} r^3 \theta_2 V_{11} \\ u_{\rm mid2} - \frac{t_{\rm h}}{2} r^3 \theta_1 V_{22} + \frac{t_{\rm h}}{2} r^3 \theta_2 V_{12} \\ u_{\rm mid3} - \frac{t_{\rm h}}{2} r^3 \theta_1 V_{23} + \frac{t_{\rm h}}{2} r^3 \theta_2 V_{13} \end{Bmatrix} \\ &= \sum_{I=1}^{\rm NP} \boldsymbol{\Psi}_I \boldsymbol{U}_I, \end{aligned} \tag{11}$$

where $u_{{\rm mid}i}$ (i=1,2,3) is the component of X_i-axis on the mid-thickness plane. V_{ik} (k=1,2,3) is a dot product of the vector $\boldsymbol{V}_i$ and the unit vector $\boldsymbol{e}_k$. $\boldsymbol{\Psi}_I$ is the displacement matrix in terms of RKs for the I-th node and is written as:

$$\boldsymbol{\Psi}_I = \sum_{I=1}^{\rm NP} \begin{bmatrix} \psi_I & 0 & 0 & -\frac{t_{\rm h}}{2} r^3 \psi_I V_{21} & \frac{t_{\rm h}}{2} r^3 \psi_I V_{11} \\ 0 & \psi_I & 0 & -\frac{t_{\rm h}}{2} r^3 \psi_I V_{22} & \frac{t_{\rm h}}{2} r^3 \psi_I V_{12} \\ 0 & 0 & \psi_I & -\frac{t_{\rm h}}{2} r^3 \psi_I V_{23} & \frac{t_{\rm h}}{2} r^3 \psi_I V_{13} \end{bmatrix}, \tag{12}$$

and $\boldsymbol{U}_I$ is coefficient vector of the I-th node, and is given by

$$\boldsymbol{U}_I = \left\{ u_{{\rm mid}1I} \; u_{{\rm mid}2I} \; u_{{\rm mid}3I} \; \theta_{1I} \; \theta_{2I} \right\}^T, \tag{13}$$

where $u_{{\rm mid}iI}$ (i=1,2,3) is the coefficient of X_i-axis displacement for I-th node on the mid-thickness plane. θ_{1I} and θ_{2I} are respectively the rotation components of the I-th node in terms of the vectors $\boldsymbol{V}_1$ and $\boldsymbol{V}_2$, which are used for the approximation of the deformation on the curved shell.

To map between Cartesian and convected coordinate systems, covariant and contravariant base vectors are introduced. The covariant base vector $\boldsymbol{G}_i$ (i=1,2,3) can be evaluated using the partial derivative of the position vector $\boldsymbol{X}$ on the mid-thickness plane:

$$\boldsymbol{G}_i = \frac{\partial \boldsymbol{X}}{\partial r^i}. \tag{14}$$

According to Eq.(6), the derivatives can be rewritten for the r^i-axis as:

$$\begin{aligned} \frac{\partial \boldsymbol{X}}{\partial r^i} &= \sum_{I=1}^{\rm NP} \frac{\partial \psi_I(r^1, r^2)}{\partial r^i} \left(\boldsymbol{X}_{{\rm mid}I} + \frac{r^3}{2} t_{\rm h} \boldsymbol{V}_{3I} \right), \quad (i = 1, 2), \\ \frac{\partial \boldsymbol{X}}{\partial r^3} &= \sum_{I=1}^{\rm NP} \psi_I(r^1, r^2) \frac{1}{2} t_{\rm h} \boldsymbol{V}_{3I}. \end{aligned} \tag{15}$$

Generally, basis vectors in the Cartesian coordinate system are orthogonal; *i.e.*, $\boldsymbol{e}_i \cdot \boldsymbol{e}_j = \delta_{ij}$. The covariant base vectors have the properties

$$\boldsymbol{G}_i \cdot \boldsymbol{G}_j \neq \delta_{ij}. \tag{16}$$

Therefore, the contravariant base vector $\boldsymbol{G}^i$ is defined to satisfy the Kronecker delta property:

$$\boldsymbol{G}_i \cdot \boldsymbol{G}^j = \delta_i^j. \tag{17}$$

The contravariant base vectors can be derived from the covariant base vectors according to Eq.(17):

$$\boldsymbol{G}^i = \frac{\boldsymbol{G}_j \times \boldsymbol{G}_k}{\boldsymbol{G}_i \cdot (\boldsymbol{G}_j \times \boldsymbol{G}_k)}, \tag{18}$$

where (i, j, k)=(1,2,3),(2,3,1),(3,1,2) in Eq.(18).

3 Meshfree discretization for linear buckling problems

The weak form of linear buckling problems can be evaluated by applying the principle of virtual work in linearized form:

$$\int_V \boldsymbol{\sigma} : \delta\boldsymbol{\varepsilon}_{\mathrm{L}} dV + \lambda \int_V \boldsymbol{\sigma}_0' : \delta\boldsymbol{\varepsilon}_{\mathrm{NL}} dV = 0, \tag{19}$$

where $\boldsymbol{\varepsilon}_{\mathrm{L}}$ and $\boldsymbol{\varepsilon}_{\mathrm{NL}}$ are the linear and nonlinear strain tensors, respectively. $\boldsymbol{\sigma}$ and $\boldsymbol{\sigma}_0'$ are the Cauchy stress tensor and pre-buckling stress tensor, respectively. δ represents the variational operator. V is the volume of the curved shell. λ is the buckling coefficient.

The total strain $\boldsymbol{\varepsilon}$ can be decomposed into linear and nonlinear terms $\varepsilon_{\mathrm{L}ij}$ and $\varepsilon_{\mathrm{NL}ij}$:

$$\begin{aligned}\boldsymbol{\varepsilon} &= \frac{1}{2}\left\{\left(\boldsymbol{G}_i \cdot \frac{\partial \boldsymbol{u}}{\partial r^j} + \boldsymbol{G}_j \cdot \frac{\partial \boldsymbol{u}}{\partial r^i}\right) + \left(\frac{\partial \boldsymbol{u}}{\partial r^i} \cdot \frac{\partial \boldsymbol{u}}{\partial r^j}\right)\right\}\boldsymbol{G}^i \otimes \boldsymbol{G}^j \\ &= \left(\varepsilon_{\mathrm{L}ij} + \varepsilon_{\mathrm{NL}ij}\right)\boldsymbol{G}^i \otimes \boldsymbol{G}^j \\ &= \boldsymbol{\varepsilon}_{\mathrm{L}} + \boldsymbol{\varepsilon}_{\mathrm{NL}}.\end{aligned} \tag{20}$$

The linear strain components $\varepsilon_{\mathrm{L}ij}$ can be derived as:

$$\varepsilon_{\mathrm{L}ij} = \begin{Bmatrix} \varepsilon_{\mathrm{L}11} \\ \varepsilon_{\mathrm{L}22} \\ 2\varepsilon_{\mathrm{L}12} \\ 2\varepsilon_{\mathrm{L}23} \\ 2\varepsilon_{\mathrm{L}31} \end{Bmatrix} = \begin{bmatrix} \boldsymbol{G}_1 \cdot \frac{\partial \boldsymbol{u}}{\partial r^1} \\ \boldsymbol{G}_2 \cdot \frac{\partial \boldsymbol{u}}{\partial r^2} \\ \boldsymbol{G}_1 \cdot \frac{\partial \boldsymbol{u}}{\partial r^2} + \boldsymbol{G}_2 \cdot \frac{\partial \boldsymbol{u}}{\partial r^1} \\ \boldsymbol{G}_2 \cdot \frac{\partial \boldsymbol{u}}{\partial r^3} + \boldsymbol{G}_3 \cdot \frac{\partial \boldsymbol{u}}{\partial r^2} \\ \boldsymbol{G}_3 \cdot \frac{\partial \boldsymbol{u}}{\partial r^1} + \boldsymbol{G}_1 \cdot \frac{\partial \boldsymbol{u}}{\partial r^3} \end{bmatrix}, \tag{21}$$

where $\partial \boldsymbol{u}/\partial r^i$ (i=1,2,3) is the derivative of the displacement vector $\boldsymbol{u}$ on the curved shell. The derivative $\partial \boldsymbol{u}/\partial r^i$ is written in matrix form as

$$\begin{aligned}\frac{\partial \boldsymbol{u}}{\partial r^i} &= \sum_{I=1}^{\mathrm{NP}} \begin{bmatrix} \frac{\partial \psi_I}{\partial r^i} & 0 & 0 & -A_{i21} & A_{i11} \\ 0 & \frac{\partial \psi_I}{\partial r^i} & 0 & -A_{i22} & A_{i12} \\ 0 & 0 & \frac{\partial \psi_I}{\partial r^i} & -A_{i23} & A_{i13} \end{bmatrix} \boldsymbol{U}_I \\ &= \sum_{I=1}^{\mathrm{NP}} \boldsymbol{\Psi}_{I,i} \boldsymbol{U}_I, \ (i = 1, 2),\end{aligned} \tag{22}$$

$$\begin{aligned}\frac{\partial \boldsymbol{u}}{\partial r^3} &= \sum_{I=1}^{\mathrm{NP}} \begin{bmatrix} 0 & 0 & 0 & -\frac{t_{\mathrm{h}}}{2}\psi_I V_{21} & \frac{t_h}{2}\psi_I V_{11} \\ 0 & 0 & 0 & -\frac{t_{\mathrm{h}}}{2}\psi_I V_{22} & \frac{t_h}{2}\psi_I V_{12} \\ 0 & 0 & 0 & -\frac{t_{\mathrm{h}}}{2}\psi_I V_{23} & \frac{t_h}{2}\psi_I V_{13} \end{bmatrix} \boldsymbol{U}_I \\ &= \sum_{I=1}^{\mathrm{NP}} \boldsymbol{\Psi}_{I,3} \boldsymbol{U}_I,\end{aligned} \tag{23}$$

where $\boldsymbol{\Psi}_{I,i}$ is the derivative of the displacement matrix $\boldsymbol{\Psi}_I$ in Eq.(12) for the r^i-axis. A_{ijk} is a dot product of a vector $\boldsymbol{A}_{ij}$ and the unit vector $\boldsymbol{e}_k$. The vector $\boldsymbol{A}_{ij}$ can be represented as:

$$\boldsymbol{A}_{ij} = \frac{t_{\mathrm{h}}}{2} r^3 \left(\frac{\partial \psi_I}{\partial r^i}\boldsymbol{V}_j + \psi_I \frac{\partial \boldsymbol{V}_j}{\partial r^i}\right). \tag{24}$$

Summarizing the above representation of the linear strain components $\varepsilon_{\mathrm{L}ij}$, the displacement-linear strain relationship is derived considering the linear strain tensor $\varepsilon_{\mathrm{L}ij}$ in Eq.(21) and the derivatives of the displacement vector in Eqs.(22) and (23). It finally yields as:

$$\begin{aligned}\varepsilon_{\mathrm{L}ij} &= \sum_{I=1}^{\mathrm{NP}} \begin{bmatrix} \boldsymbol{G}_1^T \boldsymbol{\Psi}_{I,1} \\ \boldsymbol{G}_2^T \boldsymbol{\Psi}_{I,2} \\ \boldsymbol{G}_1^T \boldsymbol{\Psi}_{I,2} + \boldsymbol{G}_2^T \boldsymbol{\Psi}_{I,1} \\ \boldsymbol{G}_2^T \boldsymbol{\Psi}_{I,3} + \boldsymbol{G}_3^T \boldsymbol{\Psi}_{I,2} \\ \boldsymbol{G}_3^T \boldsymbol{\Psi}_{I,1} + \boldsymbol{G}_1^T \boldsymbol{\Psi}_{I,3} \end{bmatrix} \boldsymbol{U}_I \\ &= \sum_{I=1}^{\mathrm{NP}} \boldsymbol{B}_{\mathrm{L}I} \boldsymbol{U}_I,\end{aligned} \tag{25}$$

where $\boldsymbol{B}_{\mathrm{L}I}$ is the displacement–linear strain matrix.

The detail of the displacement-nonlinear strain matrix $\boldsymbol{B}_{\mathrm{NL}I}$ is presented here. For convenience of representation, the vector $\boldsymbol{d}^T$ in terms of the nonlinear strain is defined as:

$$\boldsymbol{d}^T = \left\{\left(\frac{\partial \boldsymbol{u}}{\partial r^1}\right)^T \left(\frac{\partial \boldsymbol{u}}{\partial r^2}\right)^T \left(\frac{\partial \boldsymbol{u}}{\partial r^3}\right)^T\right\}. \tag{26}$$

Substituting Eq.(11) into Eq.(26) yields

$$\boldsymbol{d} = \sum_{I=1}^{\mathrm{NP}} \begin{bmatrix} \boldsymbol{\Psi}_{I,1} \\ \boldsymbol{\Psi}_{I,2} \\ \boldsymbol{\Psi}_{I,3} \end{bmatrix} \boldsymbol{U}_I = \sum_{I=1}^{\mathrm{NP}} \boldsymbol{B}_{\mathrm{NL}I} \boldsymbol{U}_I. \tag{27}$$

The stress–linear strain relationship is

$$\boldsymbol{\sigma} = \boldsymbol{C} : \boldsymbol{\varepsilon}_{\mathrm{L}}. \tag{28}$$

By employing the orthogonal unit vector $\boldsymbol{V}_i$, the stress–strain matrix $\boldsymbol{C}$ can be decomposed, as:

$$\boldsymbol{C} = C_{ijkl}\boldsymbol{V}_i \otimes \boldsymbol{V}_j \otimes \boldsymbol{V}_k \otimes \boldsymbol{V}_l. \tag{29}$$

The linear elastic matrix $\boldsymbol{C}$ can be defined in the curved shell, as:

$$\begin{aligned}\boldsymbol{C} &= \begin{bmatrix} C_{1111} & C_{1122} & C_{1112} & C_{1123} & C_{1131} \\ C_{2211} & C_{2222} & C_{2212} & C_{2223} & C_{2231} \\ C_{1211} & C_{1222} & C_{1212} & C_{1223} & C_{1231} \\ C_{2311} & C_{2322} & C_{2312} & C_{2323} & C_{2331} \\ C_{3111} & C_{3122} & C_{3112} & C_{3123} & C_{3131} \end{bmatrix} \\ &= \frac{E}{1-\nu^2}\begin{bmatrix} 1 & \nu & & & \\ & 1 & & 0 & \\ & & \frac{1-\nu}{2} & & \\ & sym. & & \kappa\frac{1-\nu}{2} & \\ & & & & \kappa\frac{1-\nu}{2} \end{bmatrix},\end{aligned} \tag{30}$$

where κ is the shear correction factor and $\kappa{=}\pi^2/12$ is taken in this work. E and ν are the Young's modulus and the Poisson's ratio, respectively. While the elastic matrix $\boldsymbol{C}$ can be represented on the curved shell based on the covariant vector $\boldsymbol{G}_i$, as:

$$\boldsymbol{C} = C^{ijkl}\boldsymbol{G}_i \otimes \boldsymbol{G}_j \otimes \boldsymbol{G}_k \otimes \boldsymbol{G}_l. \tag{31}$$

The contravariant components of the stress-strain relationship C^{ijkl} is evaluated based on Eq.(30), as:

$$C^{ijkl} = C_{mnop}(\boldsymbol{V}_m \cdot \boldsymbol{G}^i)(\boldsymbol{V}_n \cdot \boldsymbol{G}^j)(\boldsymbol{V}_o \cdot \boldsymbol{G}^k)(\boldsymbol{V}_p \cdot \boldsymbol{G}^l), \tag{32}$$

$$\sigma^{ij} = C^{ijkl}\varepsilon_{\mathrm{L}kl}. \tag{33}$$

Substituting Eqs.(25) and (27) into Eq.(19) considering the stress–strain relationship of Eq.(28), a discrete equation of the eigenvalue problem is then obtained as:

$$(\boldsymbol{K}_{\mathrm{L}} + \lambda\boldsymbol{K}_{\mathrm{NL}})\boldsymbol{U} = 0, \tag{34}$$

where $\boldsymbol{K}_{\mathrm{L}}$ and $\boldsymbol{K}_{\mathrm{NL}}$ are stiffness matrices for linear and nonlinear terms, respectively and they are expressed as

$$\boldsymbol{K}_{\mathrm{L}} = \iiint \boldsymbol{B}_{\mathrm{L}}^T\boldsymbol{C}\boldsymbol{B}_{\mathrm{L}}dV, \tag{35}$$

$$\boldsymbol{K}_{\mathrm{NL}} = \iiint \boldsymbol{B}_{\mathrm{NL}}^T\boldsymbol{\sigma}_0'\boldsymbol{B}_{\mathrm{NL}}dV, \tag{36}$$

where $\boldsymbol{B}_{\mathrm{L}}$ and $\boldsymbol{B}_{\mathrm{NL}}$ are displacement-strain matrices in the meshfree model. The volume dV can be written employing a scalar triple product of the covariant base vector $\boldsymbol{G}_i$ and a line element dr^i as:

$$dV = [\boldsymbol{G}_1\boldsymbol{G}_2\boldsymbol{G}_3]dr^1dr^2dr^3. \tag{37}$$

The pre-buckling stress tensor $\boldsymbol{\sigma}_0'$ is represented as

$$\boldsymbol{\sigma}_0' = \begin{bmatrix} \sigma_0'^{11}\boldsymbol{I} & \sigma_0'^{12}\boldsymbol{I} & \sigma_0'^{13}\boldsymbol{I} \\ \sigma_0'^{21}\boldsymbol{I} & \sigma_0'^{22}\boldsymbol{I} & \sigma_0'^{23}\boldsymbol{I} \\ \sigma_0'^{31}\boldsymbol{I} & \sigma_0'^{32}\boldsymbol{I} & \sigma_0'^{33}\boldsymbol{I} \end{bmatrix}, \tag{38}$$

where $\boldsymbol{I}$ is a 3×3 unit tensor. $\sigma_0'^{33}$ is set to be zero according to the plane stress assumption.

A nodal integration technique is introduced to accurately evaluate the stiffness matrix as defined in Eqs.(35) and (36) for the linear buckling analysis. The SCNI proposed by Chen *et al.* [58], [59] is adopted. In the meshfree discretization, a flat shell meshfree model is first arranged and a curved surface model is then generated using the convected coordinate system. The field variables are also transformed using the convected coordinate system. The detail of the SCNI for a flat shell meshfree model has been given in the literature [55]. Newton-Cotes numerical integration technique with five points is adopted in thickness direction. As for the comparison with SCNI, Gauss integration (GI) rule is adopted for derivation of the stiffness matrix. A Voronoi cell is divided a number of triangular domain and 13-point Gauss quadrature rule is adopted to evaluate Eqs.(35) and (36). The details are written in Refs.[40], [64]. The results are provided for some numerical examples.

Imposing the essential BCs in the meshfree analysis with RKs requires a special treatment because of a lack of the Kronecker delta property of the meshfree interpolants. A SK [60] is employed to introduce singularities on the nodes along the essential BCs to recover the nodal values. A standard RK is substituted with an SK along the edges where the essential BCs are imposed. By employing the SK, the essential BCs can be imposed to the limit of machine precision in the meshfree analysis.

4 Numerical examples

Buckling loads and modes for shallow shell and full cylinder models with and without cutouts are calculated to verify the accuracy and effectiveness of the present meshfree Galerkin formulation and discretization.

4.1 Meshfree modeling for curved shell geometries

The meshfree modeling of the curved structures based on the convected coordinate system is described here. For the modeling of curved shell structures, a special mapping is employed using the convected coordinate system. First, a flat shell meshfree model is created.

A mapping function is thus employed with the RKs to transform the flat shell geometry to the curved shell geometry. The curved geometry is then interpolated using the RKs. Approximation of the field variables, derivation of the stiffness matrix and numerical integration of the stiffness matrix are carried out using the flat shell model and convected coordinate system.

Meshfree modeling of different curved geometries is shown in Figs.2(a)–(f). For the shallow shell problem, a flat shell meshfree model is arranged using the scattered nodes and Voronoi cell diagram as shown in Fig.2(a). A mapping function of the shallow shell geometry is defined using the convected coordinate system, and the node positions and physical values are transformed into the shallow shell meshfree model as represented in Fig.2(b). Modeling of the full cylinder is represented in Figs.2(c) and (d). The flat shell model of Fig.2(c) can be transformed into the full cylinder model using the mapping function. After transforming the node positions onto the curved surface, the overlapped nodes located on both sides of the flat shell model are tied to satisfy continuity of the field variables in the cylinder model. All DOFs of the overlapped nodes are tied to meet the continuity of both geometry and deformations. The full cylinder meshfree model is then obtained according to the meshfree modeling as shown in Fig.2(d). The meshfree model of the perforated full cylinder model can be developed in addition to that of the full cylinder model. The models are depicted in Figs.2(e) and (f). The flat shell model including a circular cutout in Fig.2(e) can be transformed easily into the perforated cylinder geometry in Fig.2(f). The essential and traction BCs are imposed according to the curved shell geometries considering the convected coordinate system. This mapping technique is efficient in modeling an arbitral curved geometry including, for example, a cutout or through crack.

The accuracy of the meshfree models is examined in the next section. The meshfree results are compared with those of the FEM and reference solutions. In the FEM computations, the commercial FEM solver ANSYS [65] with four-noded shell elements (SHELL181), which are appropriate for analyzing thin to moderately thick shells, is chosen. In the FEM analysis convergence calculation is performed until fully converged solutions are obtained. Then, fully converged results are presented.

4.2 Buckling analysis of shallow shells

Linear buckling analyses of shallow shells are considered under simply supported and clamped conditions. The present shallow shell geometries have small curvature and convenient in the assessment of accuracy of the developed method. These shallow shells have been previously studied and can be found, for instance, in Refs.[66] and [67]. The non-dimensional critical buckling parameters presented in Ref.[68] are taken as

$$L_K = \frac{12P_{\mathrm{c}}b^2(1-\nu^2)}{E\pi^2 t_{\mathrm{h}}^2}, \tag{39}$$

and

$$Z = \frac{b^2\sqrt{1-\nu^2}}{r_{\mathrm{d}}t_{\mathrm{h}}}, \tag{40}$$

where L_K is the non-dimensional buckling coefficient divided by Young's modulus, E, while Z is the curvature parameter for the shallow shells. P_{c} is the critical stress, r_{d} is the radius of the shallow shells and b is the width of the curved side of a shell.

An illustration of the shallow shell model is schematically indicated in Fig.3. Where a is the height of the shallow shell and b is the width of the curved side of shallow shell. The plate thickness is t_{h}/b=0.015 and the Poisson's ratio is ν=0.3. The point O is the center of the cylinder diameter. (r,θ,z) denotes a point in the cylindrical coordinate system. To avoid rigid body motion, the displacements u_z at points A and B and u_θ at point C are suppressed. Two different BCs, namely the simply supported and clamped conditions, are imposed. For the simply supported condition, out-of-plane displacements (along the r-axis) on the mid-thickness plane are constrained while in-plane displacements are set to be free. Rotations about the longitudinal (z-axis) and circumferential (θ-axis) are constrained in addition to the constraints of the simply supported condition to impose the clamped conditions for the longitudinal and curved edges, respectively. Uniform pressure is applied to the top and bottom of the shallow shell.

A convergence study is performed for the problems having simply supported and clamped BCs. Curved shell models with r_{d}/b=5.0 and 17.5 and the flat shell model are considered. The convergence results of critical buckling coefficients L_K are given in Tables 1 and 2 for simply supported and clamped BCs, respectively. The error is defined as

$$Error = \frac{\mathrm{Ref.} - \mathrm{MFree}}{\mathrm{Ref.}} \times 100\ (\%). \tag{41}$$

In Eq.(41), MFree and Ref. are the results obtained by the meshfree method and the reference solutions, respectively. The solutions of Baiz and Aliabadi [66] analyzed by the boundary domain element method are chosen as reference solutions. Shell aspect ratio is taken as a/b=2.0. Nodal densities ranging from $b/20$ to $b/50$

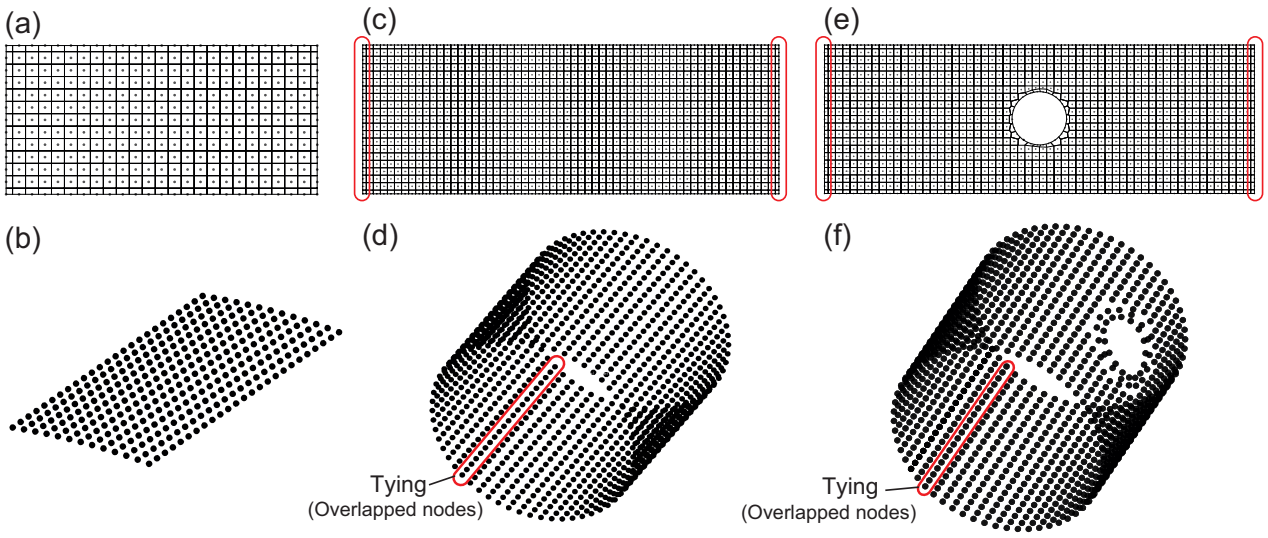

Fig. 2 Meshfree modeling based on a convected coordinate system: **a** a flat shell model for the shallow shell model, **b** a meshfree shallow shell model, **c** a flat shell model for the full cylinder model, **d** a full cylinder meshfree model, **e** a flat shell model for the perforated cylinder model, **f** a perforated full cylinder model

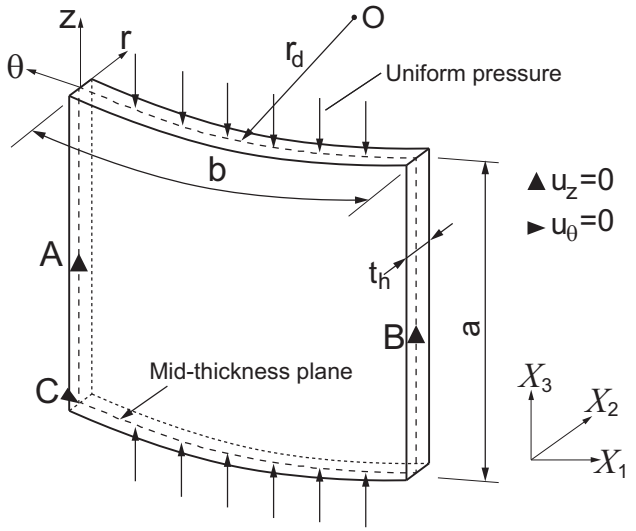

Fig. 3 Schematic representation of a shallow shell: geometry notation and its BCs

are studied. Although the reference solutions are not derived from analytical methods, converged meshfree results are obtained with good agreement with reference solutions.

Table 1 Convergence study for shallow shell problems under simply supported condition (a/b=2.0)

	Error %		
Distance	r_d/b=5.0	r_d/b=17.5	Flat
$b/20$	0.155	0.460	0.508
$b/30$	0.153	0.291	0.318
$b/40$	0.095	0.161	0.179
$b/50$	0.045	0.073	0.086

Table 2 Convergence study for shallow shell problems under clamped condition (a/b=2.0)

	Error %		
Distance	r_d/b=5.0	r_d/b=17.5	Flat
$b/20$	0.817	0.828	0.835
$b/30$	0.580	0.581	0.588
$b/40$	0.488	0.488	0.496
$b/50$	0.530	0.444	0.451

The buckling coefficients L_K of the shallow shells are further investigated to examine the effectiveness of the proposed method. The radius of curvature r_d/b is varied from 5.0 to infinity (*i.e.*, a flat shell) in case of a/b=2. The calculated results of the non-dimensional critical buckling parameters are compared with the FEM results and the reference solutions in Ref.[66]. The node density of $b/40$ is chosen in all cases. The calculated results for simply supported and clamped BCs are given in Tables 3 and 4, respectively. As expected the meshfree results are in good agreement with the FEM and reference solutions.

Table 3 Buckling coefficients L_K for shallow shells under simply supported condition (a/b=2.0)

r_d/b	Z	MFree	FEM	Ref.[66]
5.0	12.719	5.647	5.644	5.642
7.5	8.479	4.741	4.735	4.734
11.5	5.530	4.298	4.296	4.291
17.5	3.634	4.107	4.107	4.100
27.5	2.313	4.019	4.021	4.012
63.0	1.009	3.971	3.973	3.964
inf.	Flat	3.959	3.962	3.952

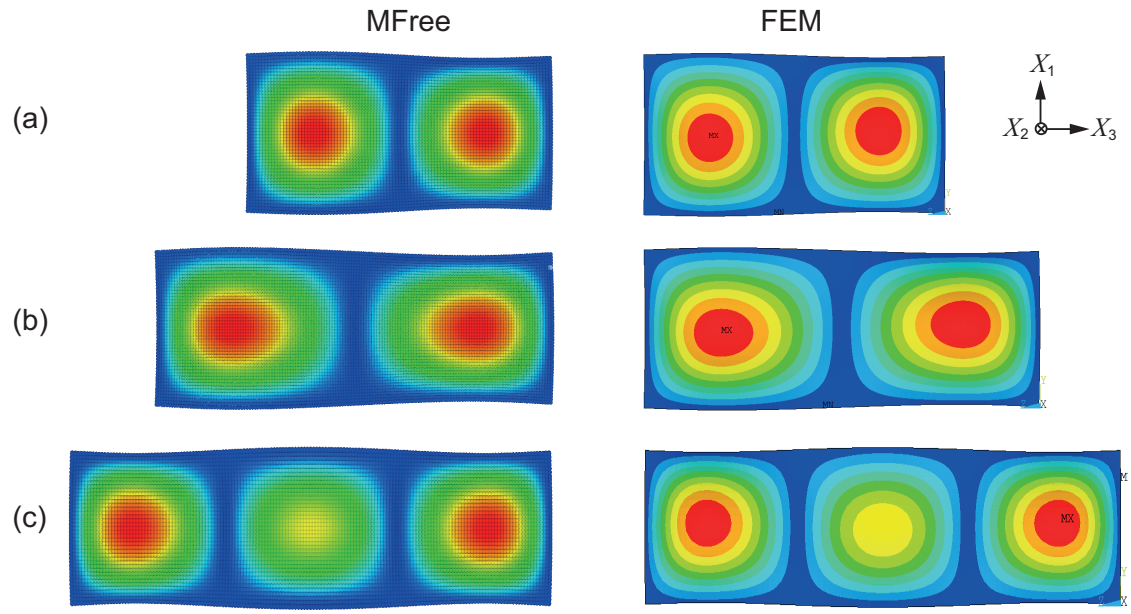

Fig. 4 Comparison of critical buckling modes of the simply supported shallow shells (r_d/b=5.0): **a** a/b=2.0, **b** a/b=3.0, **c** a/b=4.0

Table 4 Buckling coefficients L_K for shallow shells under clamped condition (a/b=2.0)

r_d/b	Z	MFree	FEM	Ref.[66]
5.0	12.719	10.351	10.337	10.402
7.5	8.479	8.942	8.953	8.985
11.5	5.530	8.294	8.311	8.334
17.5	3.634	8.021	8.042	8.060
27.5	2.313	7.897	7.920	7.936
63.0	1.009	7.829	7.853	7.868
inf.	Flat	7.813	7.836	7.852

Table 5 Buckling coefficients L_K for different aspect ratios a/b (r_d/b=5.0)

	Simply supported		Clamped	
a/b	MFree	FEM	MFree	FEM
2.0	5.647	5.644	10.351	10.337
3.0	5.779	5.742	10.014	10.005
4.0	5.676	5.639	9.920	9.914

The critical buckling loads and their modes of shells having different aspect ratios a/b are investigated for one curvature case (r_d/b=5.0). The critical buckling coefficients L_K for the shallow shell with r_d/b=5.0 are presented in Table 5 for simply supported and clamped BCs. Critical mode shapes of shells having different aspect ratios a/b are visualized in Figs.4 and 5 for simply supported and clamped BCs, respectively. We obtained symmetric mode shapes with respect to X_1- and X_3-axes by FEM and meshfree methods, the slight difference is only visualdue to the curved surfaces, which are a little difficult to visualize by same view angle. It is thus confirmed that the proposed meshfree approach employing the RK, SCNI and coordinate system is effective in treating the shallow shell problems.

4.3 Buckling analysis of full cylinder models

Buckling loads and modes of full cylinder models are studied to demonstrate the capability of the proposed technique. The problems have highly curved surfaces compared with the previous shallow shell problems. The analysis model is shown in Fig.6. The height and radius of the cylinder are denoted as L and r_d, respectively, while t_h denotes the shell thickness of the cylinder. All models are assumed to be simply supported along the compressed edges; this is realized by constraining translations in radial and circumferential directions in cylindrical coordinates. Compression is then applied to both sides. Axial displacements are assumed to be uniform along the compressed edges; this is realized by tying the displacement components of all nodes on the compressed edges in the longitudinal direction. To prevent rigid body motion of the models, points A and B are constrained in longitudinal direction as shown in Fig.6. A parametric study is performed to check the performance of the proposed technique for different lengths and perimeters of full cylinder models. The shell thickness and material properties are assumed to be the same for all models; the shell thickness t_h=10 mm, the Young's modulus E=210 GPa and the Poisson's ratio ν=0.3.

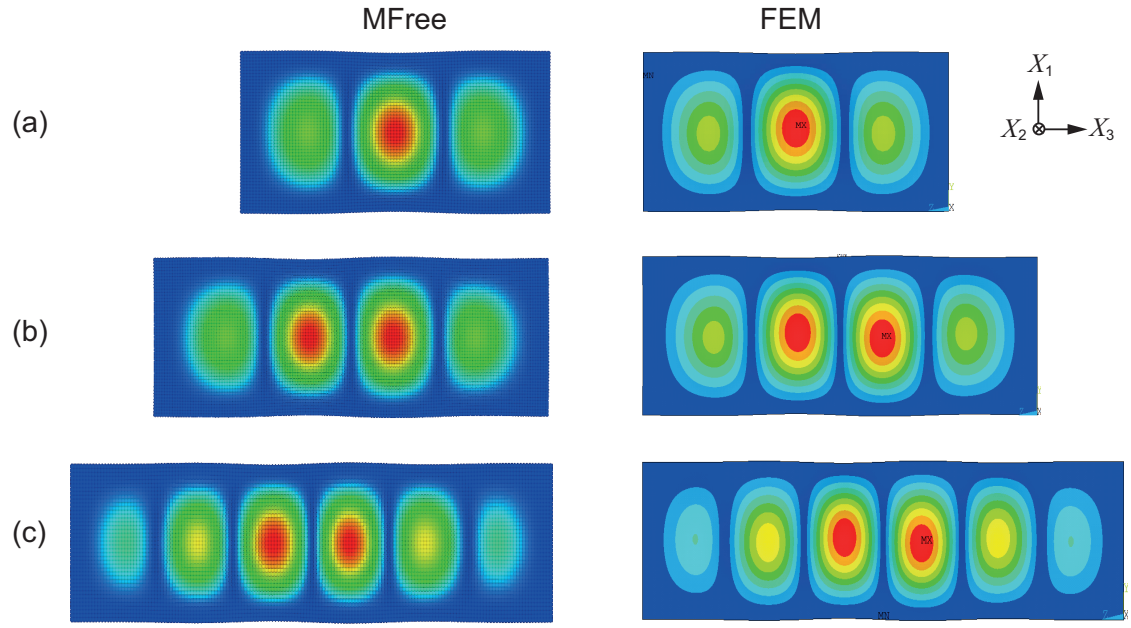

Fig. 5 Comparison critical buckling modes of the clamped shallow shells (r_d/b=5.0): **a** a/b=2.0, **b** a/b=3.0, **c** a/b=4.0

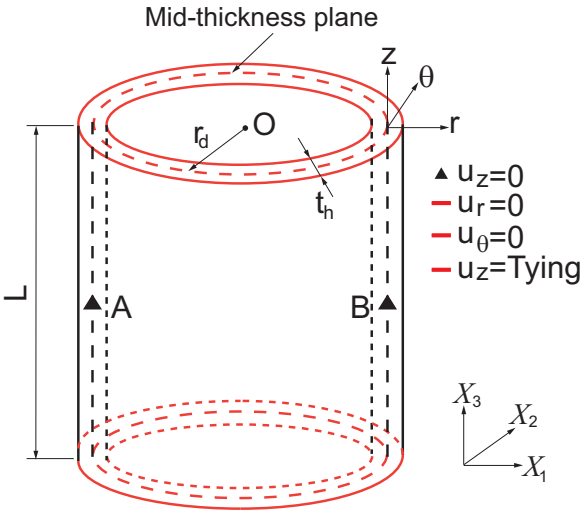

Fig. 6 Schematic representation of a full cylinder: geometry notation and its BCs

The length and perimeter are then varied. In detail, the length is set to be constant as L=1,000 mm and the perimeter is varied as b=2,500 mm and 3,000 mm. The perimeter is then assumed to be constant as b=3,000 mm and the length is varied as L=500 mm and 1,500 mm. The computed results are compared with FEM results and an analytical formula given by Ref.[69]. All the provided results are evaluated for a very fine case in which the node separations are $b/150$ for b=3,000 mm, and $b/135$ for b=2,500 mm. The critical buckling stresses of all cases are given in Table 6. In the given table the results are compared for SCNI and GI. The results are good agreement each other.

In Table 6, analytical results are calculated considering the buckling half waves in longitudinal and circumferential directions obtained by meshfree method and FEM. Buckling modes obtained by meshfree method and FEM are compared for constant length and constant perimeter cases in Figs.7 and 8, respectively.

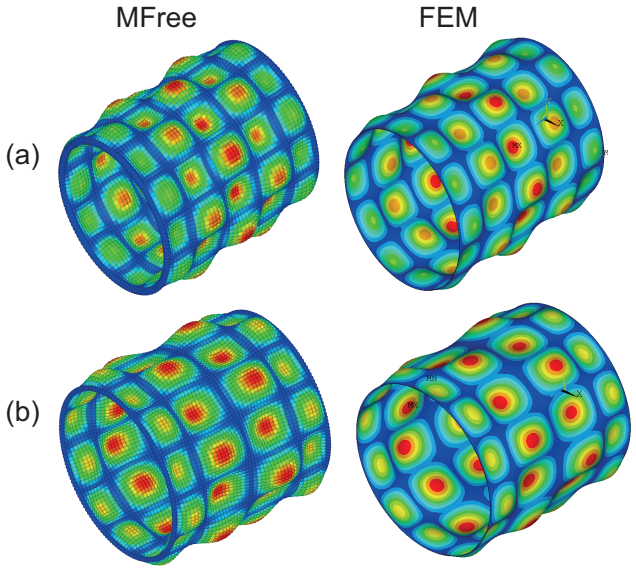

Fig. 7 Comparison of the buckling modes for L=1,000 mm: **a** b=2,500 mm, **b** b=3,000 mm

The difference between the results of the meshfree method and the analytical formula can be attributed to difference between the assumed and calculated buckling modes. In the analytical formulation in Ref.[69],

Table 6 Buckling stress for the parametric models

		kN/mm^2			
L mm	b mm	MFree (SCNI)	MFree (GI)	FEM	Analytical [69]
1,000	2,500	3.064	3.066	3.116	3.142
1,000	3,000	2.567	2.568	2.610	2.621
500	3,000	2.570	2.570	2.602	2.642
1,500	3,000	2.556	2.558	2.592	2.621

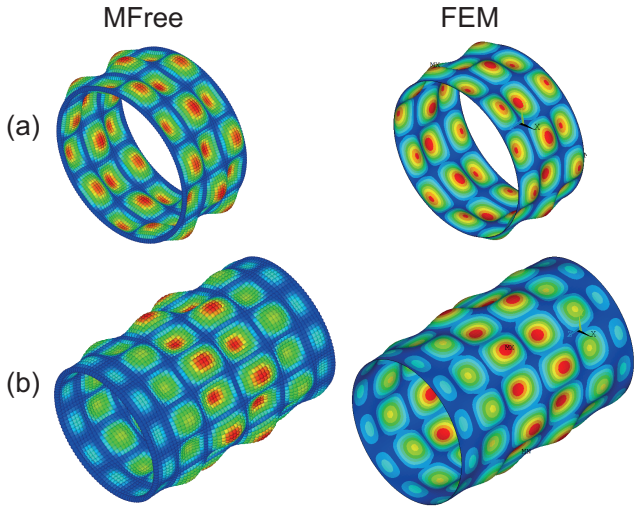

Fig. 8 Comparison of the buckling modes for b=3,000 mm: **a** L=500 mm, **b** L=1,500 mm

trigonometric functions that have uniform amplitude are adopted to represent the buckling deformations along both longitudinal and circumferential directions. However, it is seen from mode shapes by both meshfree and FEM results that the magnitudes of buckling half waves are not uniform in the longitudinal direction. Buckling half waves of smaller amplitude store less strain energy and may produce lower buckling stress compared with the analytical solutions. Meanwhile, a slight difference is observed between buckling stresses by the meshfree method and FEM. It is supposed that the difference can be attributed to the element formulation and discretization.

4.4 Buckling analysis of cylinders with circular cutouts

As the third numerical example, the dimensions are selected as L=1,000 mm and b=3,000 mm. The shell thickness, the Young's modulus and the Poisson's ratio are assumed to be the same as previous numerical examples *i.e.*, t_{h}=10 mm, E=210 GPa and ν=0.3, respectively. Hereafter, cylinders with circular cutouts are referred to as perforated cylinders for the sake of simplicity. Meshfree modeling of perforated cylinders is almost same as the modeling of full cylinders. The only difference in the models is a circular hole located at the central point of the flat plate. The same mapping and tying operations are then performed to create perforated cylinders. In addition, the same BCs used in the previous subsection are adopted for the perforated cylinders. Circular cutouts with three different radii located at the longitudinal midpoint of cylindrical shells are considered.

Computations are made using the meshfree method and FEM, and the results are then compared with the design formula for the lower bound of the buckling stress of perforated cylinders given in Ref.[70]. The lower bound of the buckling stress of perforated cylinders is obtained employing a reduction factor for the buckling stress of the intact cylindrical shells. The buckling stress of intact cylindrical shells σ_{cr} can be calculated according to classical theory as

$$\sigma_{\mathrm{cr}} = 0.605\frac{Et_{\mathrm{h}}}{r_{\mathrm{d}}}. \tag{42}$$

The reduction factor α_{c} for the lower bound buckling stress is given by

$$\alpha_{\mathrm{c}} = \frac{0.83}{\sqrt{1+2.12(r_{\mathrm{c}}/\sqrt{r_{\mathrm{d}}t_{\mathrm{h}}})^{1.4}}}, \tag{43}$$

where r_{c} is the radius of the circular cutout. The lower bound of the critical buckling stress $\sigma^{\mathrm{c}}_{\mathrm{cr}}$ of perforated cylinders is finally obtained as

$$\sigma^{\mathrm{c}}_{\mathrm{cr}} = \sigma_{\mathrm{cr}}\alpha_{\mathrm{c}}. \tag{44}$$

In the meshfree computations, the node separation is assumed as $b/150$. Both results of the meshfree method and FEM are compared with those of the design formula, and they are shown in Fig.9, in which Formula denotes the results of the lower bound of the buckling stress formula given in Ref.[70]. Good agreement is achieved between the results of the FEM and meshfree method. Additionally, both results are higher than values obtained with the lower bound design formula. From Fig.9, it is known that the critical buckling strength decreases when the cutout gets larger.

The critical mode shapes for perforated cylinders with different cutout sizes are represented in Fig.10, and good agreement is achieved between critical mode shapes obtained by meshfree method and FEM.

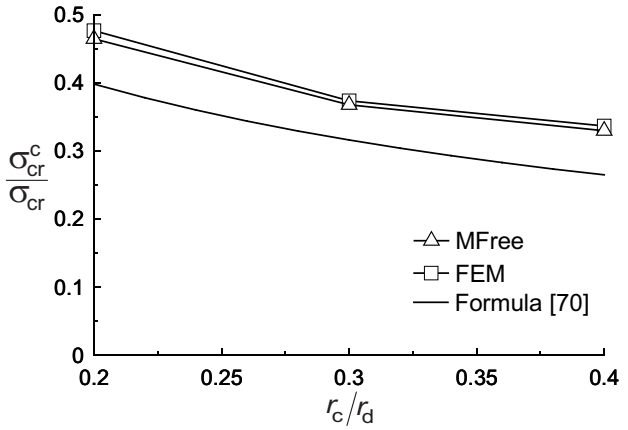

Fig. 9 Performance of the proposed technique for perforated cylinders

In the present paper, eigen value analyses including non-steep gradients deformation were treated. When analyzing buckling problems including sharp buckling modes, sub-domain stabilized conforming integration (SSCI) [47] and enrichment basis [41], [71] can be utilized.

5 Conclusions

Buckling problems for cylindrical shells were solved employing the RK meshfree method. Detailed explanation is given on the meshfree curved shell discretization, and numerical experiments of buckling for shallow and cylindrical shells with different geometries are provided. In particular, shallow shells, full cylinder models and perforated cylinder shells with circular cutouts have been studied. The calculated results of the critical buckling and mode shapes are compared with reference solutions derived from boundary domain element, FE and analytical methods. Good agreements are obtained.

The meshfree formulation based on the SCNI is efficient to prevent the occurrence of the shear locking. Essential BCs are directly imposed by employing SKs. A convected coordinate system is efficient in modeling deep or shallow shells with and without cutouts. There was good agreement between the buckling loads of the shallow shells with the results of FEM and reference solutions.

Additionally, good agreement in terms of the buckling mode shapes was also obtained. In the full cylinder case, there was good agreement in the mode shapes and stresses obtained using the FEM and analytical formula. The difference between results obtained with the proposed method and analytical formula may be attributed to the assumed and calculated buckling modes. In the analytical formulation, the amplitude of buckling half waves is assumed to be the uniform owing to the use of trigonometric functions with single deflection component to represent buckling deformations in axial direction. However, the results of the FEM and meshfree method show that amplitudes of buckling half waves are not uniform along the longitudinal axis of a cylinder. The difference between the buckling strengths obtained by FEM and meshfree method for full cylinder case is attributed to element formulation and discretization, which considerably affect the buckling strength and modes. The developed meshfree method also offers good results of buckling strength and mode shapes of the perforated cylinders as compared with the FEM solutions.

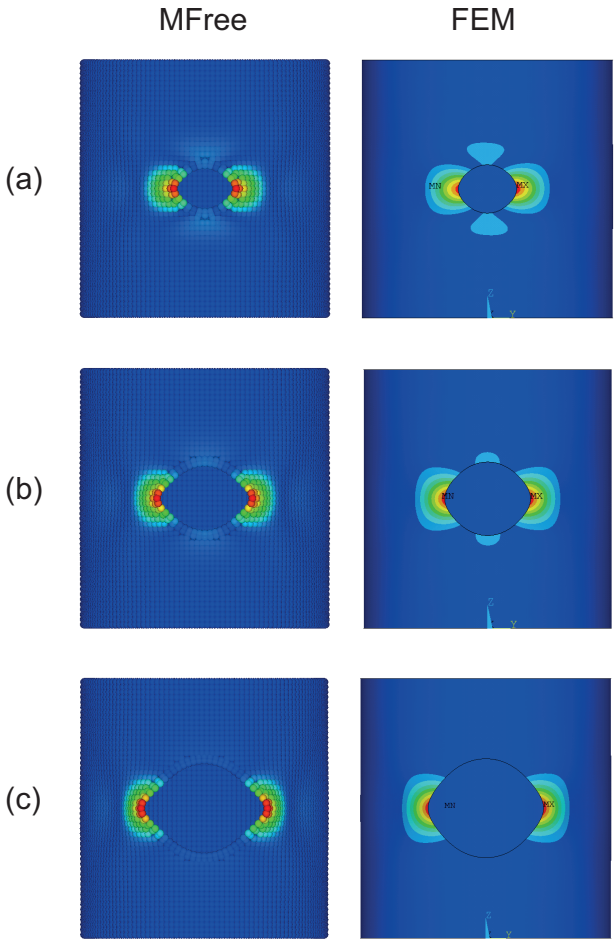

Fig. 10 Critical buckling modes for the perforated cylinder models: **a** r_c/r_d=0.2, **b** r_c/r_d=0.3, **c** r_c/r_d=0.4

6 Acknowledgement

The second author was supported by The Scientific and Technological Research Council of Turkey (TUBITAK) under 2214-A International Doctoral Research Fellowship Programme (1059B141500898), and it is gratefully

acknowledged. This research was partially supported by JSPS KAKENHI Grant-in-Aid for Scientific Research of (A)(15H02328), (B)(16H04603), (C)(15K06632).

References

1. Guggenberger W (1995) Buckling and postbuckling of imperfect cylindrical shells under external pressure. Thin Wall Struct 23:351-366
2. Jullien JF, Limam A (1998) Effects of openings of the buckling of cylindrical shells subjected to axial compression. Thin Wall Struct 31:187-202
3. Yeh MK, Lin MC, Wu WT (1999) Bending buckling of an elastoplastic cylindrical shell with a cutout. Eng Struct 21:996-1005
4. Hilburger MW, Britt VO, Nemeth MP (2001) Buckling behavior of compression-loaded quasi-isotropic curved panels with a circular cutout. Int J Solid Struct 38:1495-1522
5. Hilburger MW, Starnes Jr JH (2005) Buckling behavior of compression-loaded composite cylindrical shells with reinforced cutouts. Int J Non Lin Mech 40:1005-1021
6. Han H, Cheng J, Taheri F, Pegg N (2006) Numerical and experimental investigations of the response of aluminum cylinders with a cutout subject to axial compression. Thin Wall Struct 44:254-270
7. Shariati M, Rokhi MM (2008) Numerical and experimental investigations on buckling of steel cylindrical shells with elliptical cutout subject to axial compression. Thin Wall Struct 46:1251-1261
8. Kobayashi T, Mihara Y, Fujii F (2012) Path-tracing analysis for post-buckling process of elastic cylindrical shells under axial compression. Thin Wall Struct 61:180-187
9. Fujikubo M, Harada M, Yao T, Khedmati MR, Yanagihara D (2005) Estimation of ultimate strength of continuous stiffened panel under combined transverse thrust and lateral pressure Part 2: Continuous stiffened panel. Mar Struct 18:411-427
10. Xu MC, Yanagihara D, Fujikubo M, Soares CG (2013) Influence of boundary conditions on the collapse behaviour of stiffened panels under combined loads. Mar Struct 34:205-225
11. Tanaka S, Yanagihara D, Yasuoka A, Harada M, Okazawa S, Fujikubo M, Yao T (2014) Evaluation of ultimate strength of stiffened panels under longitudinal thrust. Mar Struct 36:21-50
12. Bayatfar A, Khedmati MR, Rigo P (2014) Residual ultimate strength of cracked steel unstiffened and stiffened plates under longitudinal compression. Thin Wall Struct 84:378-392
13. Tekgoz M, Garbatov Y, Soares CG (2015) Ultimate strength assessment of welded stiffened plates. Eng Struct 84:325-339
14. Pei Z, Iijima K, Fujikubo M, Tanaka S, Okazawa S, Yao T (2015) Simulation on progressive collapse behaviour of whole ship model under extreme waves using idealized structural unit method. Mar Struct 40:104-133
15. Yao T, Fujikubo M (2016) Buckling and ultimate strength of ship and ship-like floating structures, 1st Edition. Butterworth-Heinemann
16. Bathe KJ (1996) Finite element procedures. Prentice-Hall, Inc
17. Belytschko T, Liu WK, Moran B (2000) Nonlinear finite elements for continua and structures. John Wiley & Sons Ltd
18. Belytschko T, Lu YY, Gu L (1994) Element-free Galerkin methods. Int J Numer Meth Eng 37:229-256
19. Liu WK, Jun S, Zhang YF (1995) Reproducing kernel particle methods. Int J Numer Meth Fluid 20:1081-1106
20. Liu WK, Jun S, Li S, Adee J, Belytschko T (1995) Reproducing kernel particle methods for structural dynamics. Int J Numer Meth Eng 38:1655-1679
21. Chen JS, Pan C, Wu CT, Liu WK (1996) Reproducing kernel particle methods for large deformation analysis of non-linear structures. Comput Meth Appl Mech Eng 139:195-227
22. Chen JS, Pan C, Wu CT (1997) Large deformation analysis of rubber based on a reproducing kernel particle method. Comput Mech 19:211-227
23. Wang D, Chen P (2014) Quasi-convex reproducing kernel meshfree method. Comput Mech 54:689-709
24. Hughes TJR, Cottrell JA, Bazilevs Y (2005) Isogeometric analysis: CAD, finite elements, NURBS, exact geometry and mesh refinement. Comput Meth Appl Mech Eng 194:4135-4195
25. Bui QT (2015) Extended isogeometric dynamic and static fracture analysis for cracks in piezoelectric materials using NURBS. Comput Meth Appl Mech Eng 295:470-509
26. Yu T, Yin S, Bui QT, Xia S, Tanaka S, Hirose S (2016) NURBS-based isogeometric analysis of buckling and free vibration problems for laminated composites plates with complicated cutouts using a new simple FSDT theory and level set method. Thin Wall Struct 101:141-156
27. Yu T, Bui QT, Yin S, Doan DH, Wu CT, Do TV, Tanaka S (2016) On the thermal buckling analysis of functionally graded plates with internal defects using extended isogeometric analysis. Compos Struct 136:684-695
28. Yin S, Yu T, Bui QT, Zheng X, Tanaka S (2016) In-plane material inhomogeneity of functionally graded plates: A higher-order shear deformation plate isogeometric analysis. Compos B Eng 106:273-284
29. Tanaka S, Okada H, Okazawa S (2012) A wavelet Galerkin method employing B-spline bases for solid mechanics problems without the use of a fictitious domain. Comput Mech 50:35-48
30. Tanaka S, Okada H, Okazawa S, Fujikubo M (2013) Fracture mechanics analysis using the wavelet Galerkin method and extended finite element method. Int J Numer Meth Eng 93:1082-1108
31. Tanaka S, Suzuki H, Ueda S, Sannomaru S (2015) An extended wavelet Galerkin method with a high-order B-spline for 2D crack problems. Acta Mech 226:2159-2175
32. Tanaka S, Sannomaru S, Imachi M, Hagihara S, Okazawa S, Okada H (2015) Analysis of dynamic stress concentration problems employing spline-based wavelet Galerkin method. Eng Anal Bound Elem 58:129-139
33. Sannomaru S, Tanaka S, Yoshida K, Bui QT, Okazawa S, Hagihara S (2016) Treatment of Drichlet-type boundary conditions in the spline-based wavelet Galerkin method employing multiple point constraints. Appl Math Model 43:592-610
34. Krysl P, Belytschko T (1995) Analysis of thin plates by the element-free Galerkin method. Comput Mech 17:26-35
35. Krysl P, Belytschko T (1996) Analysis of thin shells by the element-free Galerkin method. Int J Solid Struct 33:3057-3080
36. Li S, Hao W, Liu WK (2000) Numerical simulations of large deformation of thin shell structures using meshfree methods. Comput Mech 23:102-116
37. Noguchi H, Kawashima T, Miyamura T (2000) Element free analyses of shell and spatial structures. Int J Numer Meth Eng 47:1215-1240

38. Kanok-Nukulchai W, Barry W, Saran-Yasoontorn K, Bouillard PH (2001) On elimination of shear locking in the element-free Galerkin method. Int J Numer Meth Eng 52:705-725
39. Zhang Z, Noguchi H, Chen JS (2008) Moving least-squares approximation with discontinuous derivative basis functions for shell structures with slope discontinuities. Int J Numer Meth Eng 76:1202-1230
40. Tanaka S, Suzuki H, Sadamoto S, Imachi M, Bui QT (2015) Analysis of cracked shear deformable plates by an effective meshfree plate formulation. Eng Fract Mech 144:142-157
41. Tanaka S, Suzuki H, Sadamoto S, Sannomaru S, Yu T, Bui QT (2016) *J*-integral evaluation for 2D mixed-mode crack problems employing a meshfree stabilized conforming nodal integraiton method. Comput Mech 58:185-198
42. Tanaka S, Suzuki H, Sadamoto S, Okazawa S, yu TT, Bui QT (2016) Accurate evaluation of mixed-mode intensity factors of cracked shear-deformable plates by an enriched meshfree Galerkin formulation. Arch Appl Mech doi:10.1007/s00419-016-1193-x
43. Organ D, Fleming M, Terry T, Belytschko T (1996) Continuous meshless approximations for nonconvex bodies by diffraction and transparency. Comput Mech 18:225-235
44. Krysl P, Belytschko T (1997) Element-free Galerkin method: Convergence of the continuous and discontinuous shape functions. Comput Meth Appl Mech Eng 148:257-277
45. Yiotis AJ, Katsikadelis JT (2015) Buckling of cylindrical shell panels: a MAEM solution. Arch Appl Mech 85:1545-1557
46. Wang D, Song C, Peng H (2015) A circumferentially enhanced Hermite reproducing kernel meshfree method for buckling analysis of Kirchhoff-Love cylindrical shells. Int J Struct Stabil Dynam 15:1450090
47. Wang D, Chen JS (2008) A Hermite reproducing kernel approximation for thin-plate analysis with sub-domain stabilized conforming integration. Int J Numer Meth Eng 74;368-390
48. Wang D, Lin Z (2010) Free vibration analysis of thin plates using Hermite reproducing kernel Galerkin meshfree method with sub-domain stabilized conforming integration. Comput Mech 46:703-719
49. Wang D, Lin Z (2011) Dispersion and transient analyses of Hermite reproducing kernel Galerkin meshfree method with sub-domain stabilized conforming integration for thin beam and plate structures. Comput Mech 48:47-63
50. Tanaka S, Sadamoto S, Okazawa S (2012) Large deflection analysis for thin plates using the Hermite reproducing kernel (HRK) approximation. Theor Appl Mech Jpn 60:205-214
51. Tanaka S, Sadamoto S, Okazawa S (2012) Nonlinear thin-plate bending analyses using the Hermite reproducing kernel approximation. Int J Comput Meth 9:1240012
52. Qian D, Eason T, Li S, Liu WK (2008) Meshfree simulation of failure modes in thin cylinders subjected to combined loads of internal pressure and localized heat. Int J Numer Meth Eng 76:1159-1184
53. Zhao X, Liew KM, Ng TY (2003) Vibration analysis of laminated composite cylindrical panels via a meshfree approach. Int J Solids Struct 40:161-180
54. Zhao X, Ng TY, Liew KM (2004) Free vibration of two-side simply-supported laminated cylindrical panels via the mesh-free kp-Ritz method. Int J Mech Sci 46:123-142
55. Sadamoto S, Tanaka S, Okazawa S (2013) Elastic large deflection analysis of plates subjected to uniaxial thrust using meshfree Mindlin-Reissner formulation. Comput Mech 52:1313-1330
56. Sadamoto S, Tanaka S, Okazawa S (2014) Buckling analysis of plate with an initial imperfection using RKPM based on convected coordinate system. Journal of the JASNAOE 19:169-178 (in Japanese)
57. Sadamoto S, Yoshida K, Tanaka S (2015) Modeling of plate structures for Galerkin meshfree methods (2nd report: Geometrical non-linear analysis). Trans. of the JSME 81:15-00252 (in Japanese)
58. Chen JS, Wu CT, Yoon S, You Y (2001) A stabilized conforming nodal integration for Galerkin mesh-free methods. Int J Numer Meth Eng 50:435-466
59. Chen JS, Yoon S, Wu CT (2002) Non-linear version of stabilized conforming nodal integration for Galerkin mesh-free methods. Int J Numer Meth Eng 53:2587-2615
60. Chen JS, Wang HP (2000) New boundary condition treatments in meshfree computation of contact problems. Comput Meth Appl Mech Eng 187:441-468
61. Wang D, Sun Y (2011) A Galerkin meshfree method with stabilized conforming nodal integration for geometrically nonlinear analysis of shear deformable plates. Int J Comput Meth 8:685
62. Wang D, Chen JS (2004) Locking-free stabilized conforming nodal integration for meshfree Mindlin-Reissner plate formulation. Comput Meth Appl Mech Eng 193:1065-1083
63. Wang D, Chen JS (2006) A locking-free meshfree curved beam formulation with the stabilized conforming nodal integration. Comput Mech 39:83-90
64. Sadamoto S, Tanaka S, Okazawa S (2013) A study for numerical integration technique of plate bending analysis employing meshfree approach. Transactions of JSCES Paper No. 20130008 (in Japanese)
65. ANSYS (2013), User's manual release 14.5
66. Baiz PM, Aliabadi MH (2006) Linear buckling analysis of shear deformable shallow shells by the boundary domain element method. Comput Model Eng Sci 13:19-34
67. Baiz PM, Aliabadi MH (2007) Buckling analysis of shear deformable shallow shells by the boundary element method. Eng Anal Bound Elem 31:361-372
68. Gerard G, Becker H (1957) Handbook of structural stability part III-buckling of curved plates and shells. NACA TN 3783.
69. Marcinowski J (2010) Buckling resistance assessment of a slender cylindrical shell axially compressed. Mech Mech Eng 14:309-316
70. Eggwertz S, Samuelson LA (1991) Design of shell structures with openings subjected to buckling. J Constr Steel Res 18:155-163
71. Joyot P, Trunzler J, Chinesta F (2005) Enriched reproducing kernel approxiation: Reproducing functions with discontinuous derivatives. Lecture Notes in Comput Sci and Eng 43:93-107